Supplementary material to "Time-reversal symmetry breaking in the new noncentrosymmetric superconductor Zr_3Ir"

T. Shang,[1,*] S. K. Ghosh,[2,†] J. Z. Zhao,[3] L.-J. Chang,[4] C. Baines,[5] M. K. Lee,[4] D. J. Gawryluk,[1] M. Shi,[6] M. Medarde,[1] J. Quintanilla,[2] and T. Shiroka[7,8]

[1] *Laboratory for Multiscale Materials Experiments, Paul Scherrer Institut, Villigen CH-5232, Switzerland*
[2] *School of Physical Sciences, University of Kent, Canterbury CT2 7NH, United Kingdom*
[3] *Co-Innovation Center for New Energetic Materials, Southwest University of Science and Technology, Mianyang, 621010, People's Republic of China*
[4] *Department of Physics, National Cheng Kung University, Tainan 70101, Taiwan*
[5] *Laboratory for Muon-Spin Spectroscopy, Paul Scherrer Institut, CH-5232 Villigen PSI, Switzerland*
[6] *Swiss Light Source, Paul Scherrer Institut, Villigen CH-5232, Switzerland*
[7] *Laboratorium für Festkörperphysik, ETH Zürich, CH-8093 Zurich, Switzerland*
[8] *Paul Scherrer Institut, CH-5232 Villigen PSI, Switzerland*

Crystal structure

Polycrystalline Zr_3Ir samples were prepared by arc melting of Zr and Ir metals in a water-cooled copper hearth under high-purity argon atmosphere. The as-cast ingots were then annealed at 600°C over two weeks. The crystal structure and the purity of Zr_3Ir were checked via x-ray powder diffraction (XRD) at room temperature. Rietveld refinements indicate a tiny amount ($< 3\%$) of a Zr impurity phase. As shown in Fig. S1, the XRD pattern of Zr_3Ir can be adequately indexed by a tetragonal α-V_3S-type noncentrosymmetric structure with space group $I\bar{4}2m$ (No. 121). The resulting lattice parameters are $a = b = 10.78628(5)$ Å and $c = 5.65891(4)$ Å. The twice as large in-plane vs. out-of-plane lattice parameter hints at an anisotropic crystal structure. As shown in the inset, the refined Zr_3Ir crystal structure includes three different Zr sites and a single Ir site in the unit cell. The detailed atomic positions presented in Table SI are consistent with previously reported values [1].

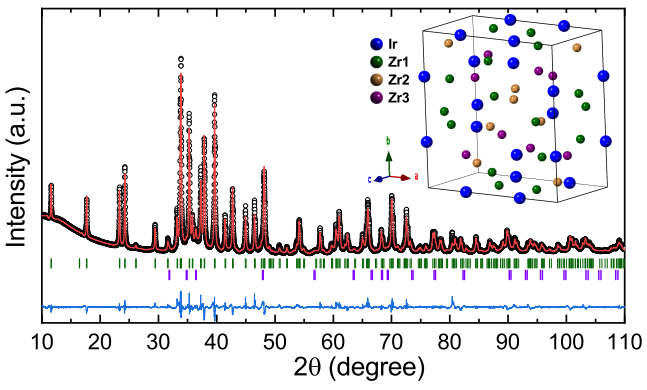

FIG. S1. Room-temperature x-ray powder diffraction pattern and relevant Rietveld refinements for Zr_3Ir. Black symbols refer to the experimental data, while the red line to the refined profile. The rows of green and purple ticks under the pattern indicate the positions of Bragg reflections for Zr_3Ir and Zr, respectively, while the blue line shows the residuals (difference between the refined and experimental patterns). The inset shows the crystal structure of Zr_3Ir.

Table SI. The refined crystal-lattice parameters and atomic coordinates of Zr_3Ir at room temperature. The derived profile reliability factor is $R_p = 3.77\%$ and the weighted-profile R-factor is $R_{wp} = 5.14\%$.

Structure	α-V_3S-type tetragonal
Space group	$I\bar{4}2m$ (No. 121)
a(Å)	10.78628(5)
c(Å)	5.65891(4)
V_{cell}(Å^3)	658.378(6)

Atomic coordinates

Atom	Wyckoff	Occ.	x	y	z
Ir	$8f$	1	0.29122(7)	0	0
Zr_1	$8g$	1	0.35316(11)	0	0.5
Zr_2	$8i$	1	0.09685(13)	0.09685(13)	0.25874(35)
Zr_3	$8i$	1	0.29163(11)	0.29163(11)	0.25595(72)

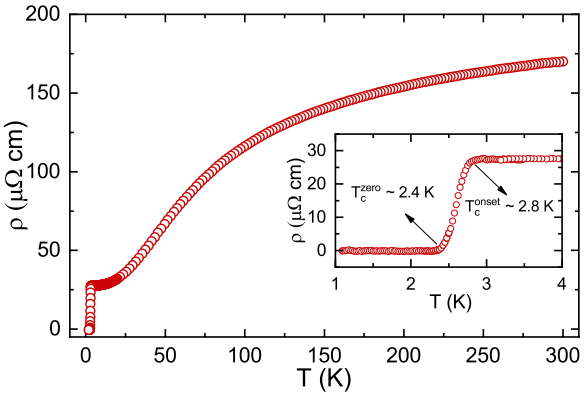

FIG. S2. Electrical resistivity vs. temperature for Zr_3Ir, measured in the 1–300 K temperature range in absence of magnetic fields. The inset expands the low-T region, with the arrows indicating the onset- and the zero superconducting-transition temperatures, respectively.

Electrical resistivity

Figure S2 shows the temperature dependence of the zero-field electrical resistivity $\rho(T)$ for Zr_3Ir. In the covered temperature range, $\rho(T)$ suggests a metallic behavior, characterized by a residual resistivity of 27 $\mu\Omega$ cm

and a residual resistivity ratio $RRR \sim 6.3$. The moderately large RRR value indicates a good Zr_3Ir sample quality. The inset expands the low-temperature region to better show the superconducting transition. As highlighted by the arrows, Zr_3Ir becomes a superconductor below $T_c^{\rm onset} \sim 2.8\,$K and its electrical resistivity drops

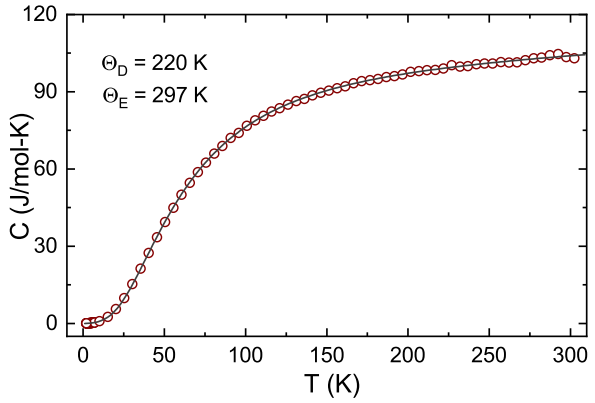

FIG. S3. Temperature dependence of the zero-field heat capacity of Zr_3Ir in the 1.9–300 K temperature range. The solid line represents a combined Debye-Einstein fit to the experimental data.

to zero at $T_c^{\rm zero} \sim 2.4\,$K. The latter value is consistent with the onset of superconductivity as determined from magnetic susceptibility measurements (see Fig. 1 in the main text).

Heat capacity

The high-temperature heat-capacity data presented in Fig. S3 show the clear dominance of phonon contribution. The solid line suggests that experimental data are well fitted by a combined Debye- and Einstein model, respectively describing the acoustic and optical phonon modes:

$$C = \gamma_{\rm n} + n_{\rm D} C_{\rm D}(T, \Theta_{\rm D}) + n_{\rm E} C_{\rm E}(T, \Theta_{\rm E}). \qquad (1)$$

Here $\gamma_{\rm n}$ is the normal-state electronic specific-heat coefficient, fixed to the value derived from the normal-state data just above T_c [see Fig 2(c) in the main text]. $C_{\rm D}$ and $C_{\rm E}$ represent the Debye- and Einstein phonon contributions, with weights $n_{\rm D} = 0.81$ and $n_{\rm E} = 0.19$, and with Debye- and Einstein temperatures $\Theta_{\rm D} = 220(5)\,$K and $\Theta_{\rm E} = 297(10)\,$K, respectively. The Debye temperature is similar to that calculated using the β value [$\Theta_{\rm D} = (12\pi^4\, Rn/5\beta)^{1/3} = 190(3)\,$K] in Fig. 2(c) of the main text, with R the molar gas constant and $n = 4$ the number of atoms per formula unit.

The density of states at the Fermi level $N(\varepsilon_{\rm F})$ can be estimated from the expression $N(\varepsilon_{\rm F}) = 3\gamma_{\rm n}/(2\pi^2 k_{\rm B}^2)$ (accounting for spin degeneracy), where $k_{\rm B}$ and $\gamma_{\rm n}$ are the Boltzmann constant and the normal-state electronic specific-heat coefficient, respectively [2]. For Zr_3Ir, a $\gamma_{\rm n} = 17.9(1)\,$mJ/mol-K^2 gives $N(\varepsilon_{\rm F}) = 3.80(1)\,$states/(eV f.u). The electron-phonon coupling constant $\lambda_{\rm ep}$ can be further estimated from $\Theta_{\rm D}$ and T_c by applying the empirical McMillan formula [3]:

$$\lambda_{\rm ep} = \frac{1.04 + \mu^* \ln(\Theta_{\rm D}/1.45\,T_c)}{(1 - 0.62\,\mu^*)\ln(\Theta_{\rm D}/1.45\,T_c) - 1.04}. \qquad (2)$$

With a bulk $T_c = 2.2(1)\,$K, $\Theta_D = 220(5)\,$K, and by considering the Coulomb-repulsion strength μ^* in the typical 0.09–0.18 range, the estimated $\lambda_{\rm ep} = 0.47$–0.67 implies a weak-coupling superconductivity in Zr_3Ir. Such weak coupling is further confirmed by the superconducting gap to critical temperature ratio ($2\Delta/k_{\rm B}T_c \sim 3.24$) and by the specific-heat jump at T_c ($\Delta C/\gamma T_c \sim 1.32$), both of which are comparable with BCS values.

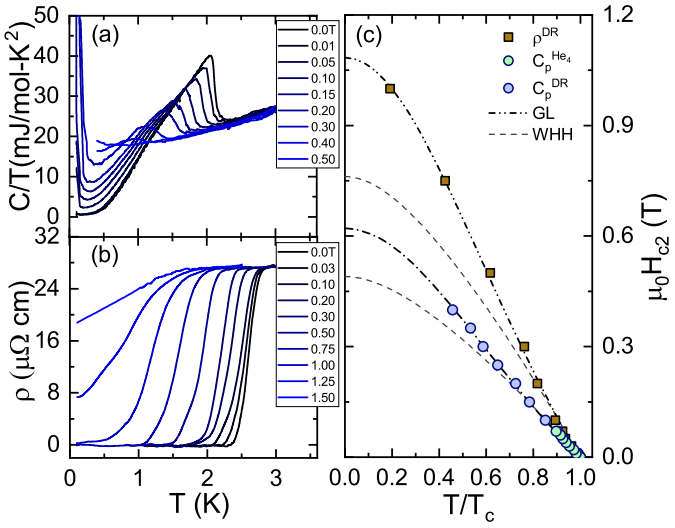

FIG. S4. Temperature dependence of (a) specific heat, and (b) electrical resistivity of Zr_3Ir in various magnetic fields up to 1.5 T. (c) Upper critical field $\mu_0 H_{c2}$ vs. normalized temperature T/T_c. Dashed-dotted lines represent fits to the GL model, while dashed-lines are fits to the WHH model considering only the orbital limit.

Upper critical field

To calculate the magnetic penetration depth from the $\mu_0 H_{c1}$ and μSR depolarization data, the upper critical field $\mu_0 H_{c2}$ had also to be determined. This was done by measuring the specific heat $C(T)/T$ and the electrical resistivity $\rho(T)$ at various magnetic fields up to 1.5 T. As shown in Fig. S4(a), $C(T)/T$ data at zero field indicate a bulk T_c of 2.2 K, consistent with the magnetic susceptibility results. Upon increasing the magnetic field, the superconducting transition in both cases shifts towards lower temperatures. Similar to other Ir-based intermetallic compounds [4], the remarkable specific-heat upturn at low temperatures is due to nuclear Schottky contributions. The derived upper critical fields $\mu_0 H_{c2}$ vs. the normalized temperature T/T_c were further analyzed by using the Ginzburg-Landau- (GL) and the Werthamer-Helfand-Hohenberg (WHH) model [5, 6]. The remarkable agreement of the GL model with the data is clearly seen in Fig. S4(c). Both models fit very well the experimental data at low fields. However, at high applied fields, the WHH model deviates significantly from the experiments, thus underestimating the critical-field values as

determined from C/T and ρ [$\mu_0 H_{c2}^{\rm WHH}(0) = 0.49(1)$ T and 0.76(1) T, respectively]. At the same time, the GL model is a good fit over the entire field range, providing $\mu_0 H_{c2}^{\rm GL}(0) = 0.62(1)$ T (C/T) and 1.08(1) T (ρ), respectively. We note that while both data sets agree well at low fields (< 0.08 T), at high fields the transition temperatures determined from $\rho(T)$ data are systematically higher than those derived from $C(T)/T$. A similar behavior has been found also in other NCSCs, e.g., LaPtSi, BiPd, or LaTSi$_3$(T = Pd, Pt, and Ir) [7–11]. Here, surface/filamentary superconductivity above bulk T_c, or a strong anisotropy of the upper critical field due to a significant c/a crystal anisotropy, have been proposed to justify the differing T_c values. In the main text, the bulk $\mu_0 H_{c2}$ value determined from specific heat was used. The coherence length ξ can be calculated from $\xi = \sqrt{\Phi_0/2\pi\, H_{c2}}$, where $\Phi_0 = 2.07\times10^{-3}$ T μm^2 is the quantum of magnetic flux. With a bulk $\mu_0 H_{c2} = 0.62(1)$ T, the calculated $\xi(0)$ is 23.0(2) nm. By using the expression $\mu_0 H_{c1} = (\Phi_0/4\pi\lambda^2)[\ln(\kappa) + 0.5)]$, where $\kappa = \lambda/\xi$ is the GL parameter, the resulting penetration depth is $\lambda_{\rm GL} =$ 182(2) nm, somewhat smaller than 294(2) nm, the experimental value from TF-μSR data. Such discrepancy most likely reflects the anistropy of Zr$_3$Ir.

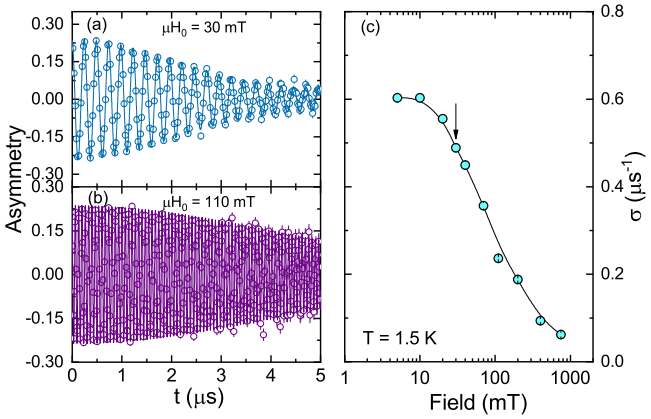

FIG. S 5. Time-domain TF-μSR spectra in the superconducting state of Zr$_3$Ir measured at (a) 30 and (b) 110 mT. (c) Above the lower critical field $\mu_0 H_{c1}$ (12.7 mT), the field-dependent Gaussian relaxation rate decreases continuously. The arrow indicates the field value used in the temperature-dependent TF-μSR studies. The solid line is a guide to the eyes.

TF-μSR

The optimal field value to employ in the TF-μSR studies of Zr$_3$Ir was determined via preliminary field-dependent μSR depolarization-rate measurements at 1.5 K. Figures S5(a) and (b) show the TF-spectra in an applied field of 30 and 110 mT, respectively. The solid lines represent fits using the same model as that in Eq. (1) of the main text. The resulting Gaussian relaxation rate $\sigma(H)$ [see Fig. S5(c)] exhibits a clear decrease above 20 mT, which is close to the lower critical field $\mu_0 H_{c1}$ = 12.7 mT (see Fig. 1 in the main text). By considering the decrease of intervortex distance with the field and the vortex-core effects, a field of 30 mT was chosen for the temperature-dependent TF-μSR studies.

ZF-μSR

To clearly explain the difference ZF-μSR results between present and previous work, we plot the temperature dependence of ZF-μSR relaxation rates $\Lambda(T)$ in Fig. S6. As can be seen in Fig. S6, the deviation of the refined relaxation rates $\Lambda(T)$ from Ref. 12, with typical value of $\sim$0.01 μs^{-1}, is even greater than the small yet systematic increase in the relaxation rate reported in present work. The largest difference below and above T_c in our data sets is less than 0.008 μs^{-1}. Therefore, the subtle signature of TRS breaking would not have been seen in the previous studies due to a lack of sufficient time resolution.

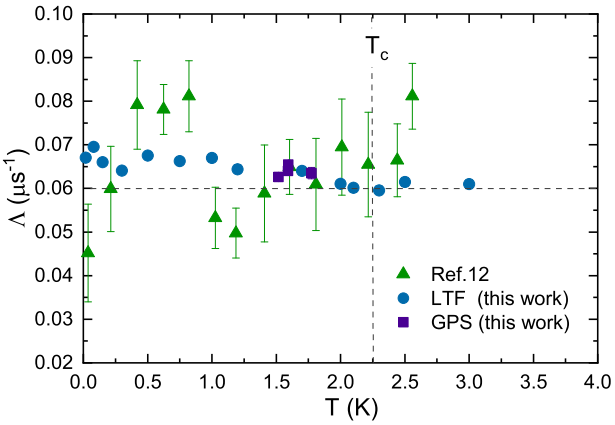

FIG. S6. ZF-μSR relaxation rate $\Lambda(T)$ vs. temperature for Zr$_3$Ir. Circles and squares are data from present work, while triangles are data adopted from recently published paper [12]. Our data sets were shifted by a constant value 0.05 μs^{-1}. The dashed lines are guides to the eye.

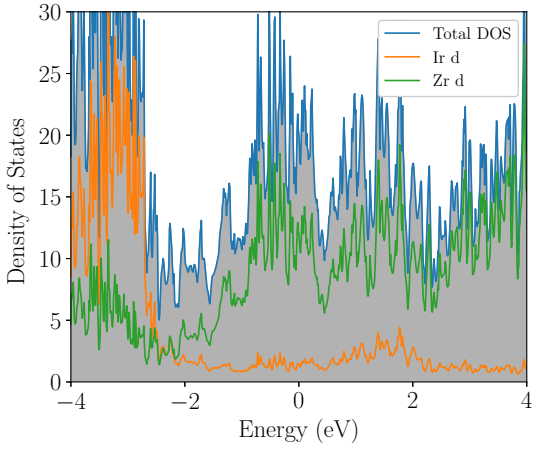

FIG. S7. Total- and single-atom projected DOS (in units of states/eV) of Zr$_3$Ir within a $\pm$4 eV energy range across $E_{\rm F}$. The results shown here do not consider the SOC.

Electronic band structure

The electronic band structure of Zr_3Ir, as shown in Fig.4 of the main text, was calculated by the density functional theory (DFT) within the generalized gradient approximation (GGA)[13] with Perdew-Burke-Ernzerhof (PBE) realization as implemented in the Vienna ab-initio Simulation Package (VASP)[14, 15]. The projector augmented wave (PAW)[16, 17] pseudopotentials are adopted for the calculation. We set 9 electrons ($5d^7 6s^2$) for Ir, and 4 electrons ($4d^2 5s^2$) for Zr as valence electrons. The kinetic energy cutoff is fixed to 500 eV. The Brillouin zone integration was performed on a Γ-centered mesh of $10 \times 10 \times 10$ k-points for the bulk calculation. The spin-orbit coupling (SOC) effect is taken into account by using a scalar relativistic approximation. The experimental lattice parameters and atomic positions determined from the Rietveld refinements (see Fig. S1) are used in our calculation.

The calculated electronic density of states (DOS) is presented in Fig. S7, without considering the spin-orbit coupling (SOC). We note that the DOS near the Fermi level consists mostly of Zr and Ir d-bands, the contribution of s-bands being negligible. Since the atomic ratio between Zr and Ir is 3:1, the Zr d-bands are expected to contribute most of the DOS at Fermi level and thus the band splitting is relatively small. The Ir atom has much stronger SOC strength to Zr, reflecting the fact that the Ir is $5d$ metal while Zr is $4d$ metal. The estimated DOS at E_F is about 2 states/(eV f.u.) [= 16 states/(eV cell)/Z, with $Z = 8$ the number of Zr_3Ir formula units per unit cell], which is comparable to the experimental results in Fig. S3.

In Fig. S8, we show several representative Fermi surfaces of Zr_3Ir, obtained without considering the SOC (see above). Note that all the Fermi surfaces are open along the two "poles". Figure S9(a) shows the contribution of these Fermi surfaces to the DOS near the Fermi level, with the relative weights being summarized in Fig. S9(b). Clearly, the Fermi surfaces in the panels (b), (c), (d), and (e) of Fig. S8 contribute to the majority of the DOS near the Fermi level E_F.

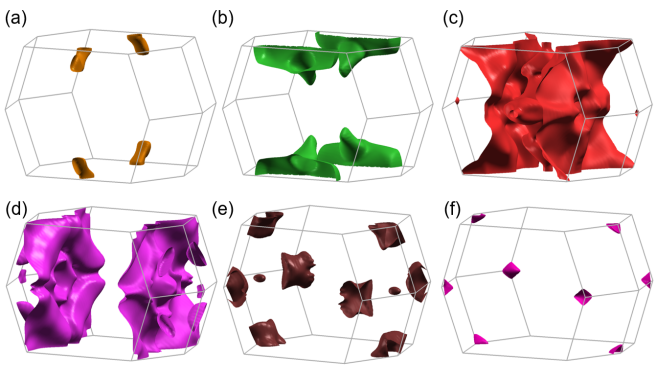

FIG. S8. Representative Fermi surfaces of Zr_3Ir neglecting the effect of SOC.

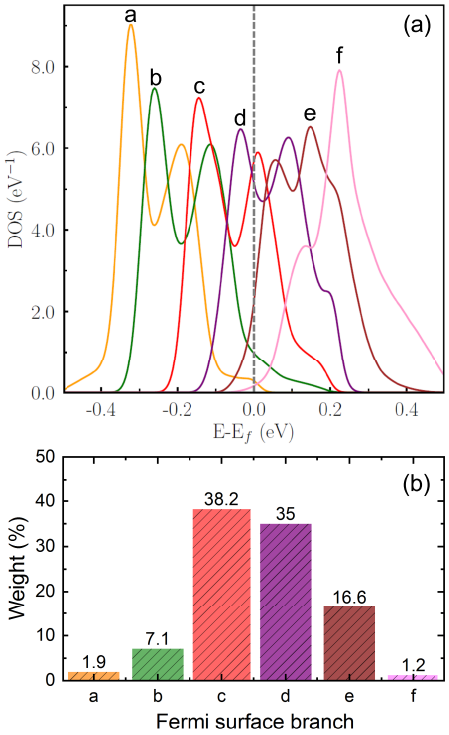

FIG. S9. (a) The contribution to the DOS of the individual Fermi surfaces shown in Fig. S8 following the same color code. (b) The relative weights of the DOS contributions of each Fermi surfaces in Fig. S8 (a) to (f) to their total DOS at E_F.

Table SII. Basis functions of D_{2d}. A, B, and C are constants independent of $\mathbf{k}$.

D_{2d}	Basis functions	
Irreps	Scalar (even)	Vector (odd)
A_1	$A + B(k_x^2 + k_y^2) + Ck_z^2$	$A(k_x\hat{x} - k_y\hat{y}) + Bk_z(k_x^2 - k_y^2)\hat{z}$
A_2	$Ak_xk_y(k_x^2 - k_y^2)$	$A(k_x\hat{x} + k_y\hat{y}) + Bk_xk_yk_z\hat{z}$
B_1	$A(k_x^2 - k_y^2)$	$A(k_x\hat{x} + k_y\hat{y}) + Bk_z\hat{z}$
B_2	Ak_xk_y	$A(k_z^2 - k_y^2)k_y\hat{x} - (k_z^2 - k_x^2)k_x\hat{y}$
E	$Ak_z \begin{pmatrix} k_x \\ k_y \end{pmatrix}$	$\begin{pmatrix} Ak_z\hat{x} + Bk_x\hat{z} \\ Ak_z\hat{y} + Bk_y\hat{z} \end{pmatrix}$

Symmetry analysis

In this section we provide details of the symmetry analysis of possible superconducting order parameters in Zr_3Ir. Due to the nontrivial effect of SOC in such compound, Zr_3Ir shows a mixed singlet- and triplet pairing in its superconducting state. The most relevant basis functions of the corresponding point group D_{2d} for this case are listed in Table. SII. D_{2d} has four non-degenerate (1D) and one degenerate (2D) irreducible representations (irreps). The singlet-dominated superconducting instability, corresponding to the 2D irrep, can be obtained by taking

$$\Delta_0(\mathbf{k}) = (\eta_1 k_z k_x + \eta_2 k_z k_y)\,, \tag{3}$$

where η_1 and η_2 are complex coefficients. Then, by minimizing the corresponding GL free energy up to the quartic order, we obtain the possible ground states: $(\eta_1, \eta_2) = (1, 0)$, $(1, 1)$, and $(1, i)$. As described in the main text, the ground state corresponding to $(\eta_1, \eta_2) = (1, i)$ breaks the

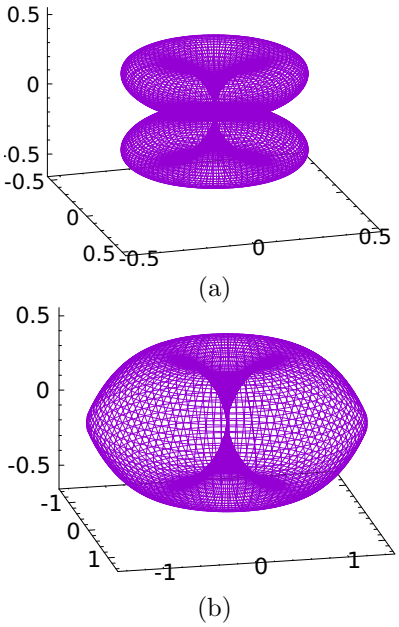

FIG. S10. Polar plots of the lowest excitation gaps singlet dominated (a) and triplet dominated (b) TRS-breaking instabilities. In both the cases point nodes appear at the "poles", while the singlet case has an additional line node at the "equator".

TRS. The corresponding lowest excitation gap is shown in Fig. S10(a). Similarly, the gap corresponding to the triplet dominated TRS breaking described in the main text is shown in Fig. S10(b). Note that the TRS breaking SC instability corresponding to these two ground states requires additional crystalline symmetry breaking and hence the pairing mechanism is necessarily unconventional (i.e., not phonon-mediated).

We compute the excitation spectrum for a general order parameter of mixed parity by using the Bogoliubov-de Gennes formalism. The relevant Hamiltonian can be written as:

$$\mathcal{H} = \begin{pmatrix} \hat{h}(\mathbf{k}) & \hat{\Delta}(\mathbf{k}) \\ \hat{\Delta}^\dagger(\mathbf{k}) & -\hat{h}^T(-\mathbf{k}) \end{pmatrix}, \tag{4}$$

where $\hat{h}(\mathbf{k})$ is the single-particle Hamiltonian. For a non-centrosymmetric material, in general, we can write

$$\hat{h}(\mathbf{k}) = (\varepsilon_{\mathbf{k}} - \mu) \cdot \mathbf{1} + \boldsymbol{\gamma}_{\mathbf{k}} \cdot \boldsymbol{\sigma}, \tag{5}$$

where μ is the chemical potential of the system, $\varepsilon_{\mathbf{k}}$ is the single-particle dispersion, and $\boldsymbol{\gamma}_{\mathbf{k}}$ is the ASOC constant which fulfills the condition $\boldsymbol{\gamma}_{\mathbf{k}} = -\boldsymbol{\gamma}_{-\mathbf{k}}$. The simplest form of the normal-state band structure compatible with the symmetry of the crystal can be assumed to be:

$$\varepsilon_{\mathbf{k}} = A_3 + B_3(k_x^2 + k_y^2) + C_3 k_z^2, \tag{6}$$

$$\boldsymbol{\gamma}_{\mathbf{k}} = A_4(k_x\hat{x} - k_y\hat{y}) + B_4 k_z(k_x^2 - k_y^2)\hat{z}, \tag{7}$$

corresponding to the A_1 irrep of D_{2d} (see Table. SII) with A_3, B_3, C_3, A_4 and B_4 being constants independent of $\mathbf{k}$. The lowest excitation spectrum on the Fermi level in general has two point nodes, at the "north" and "south" poles, corresponding to $\theta = 0$ and π, respectively. As discussed in the main text, a line node at the "equator" ($\theta = \pi/2$) is also possible when the system exhibits mostly a singlet pairing (for $A_1 \gg A_2$ and $A_1 \gg B_2$).

A qualitatively different superconducting instability, which can break TRS spontaneously at the superconducting transition, is given by the loop-super-current (LSC) ground state [18]. This is possible in Zr_3Ir because of its multi-band nature and, more specifically, because its bands are derived from several distinct but symmetry-related sites within the unit cell. By considering on-site singlet paring, with the possibility that the pairing potential can have different values at different symmetrically distinct sites, we can construct the GL free energy in the real space. By using the symmetry operations of the point group D_{2d}, we can construct the inverse pairing susceptibility matrix $\hat{\alpha}$ of the system. It can be parametrized by three real parameters p_1, p_2, and p_3:

$$\hat{\alpha} = \begin{pmatrix} p_1 & p_2 & p_3 & p_3 \\ p_2 & p_1 & p_3 & p_3 \\ p_3 & p_3 & p_1 & p_2 \\ p_3 & p_3 & p_2 & p_1 \end{pmatrix}. \tag{8}$$

This has two non-degenerate eigenvalues $(p_1 + p_2 - 2p_3)$ and $(p_1 + p_2 + 2p_3)$ and a two-fold degenerate eigenvalue $(p_1 - p_2)$, with corresponding eigenvectors

$$|1\rangle = \begin{pmatrix} 0 \\ 0 \\ -1 \\ 1 \end{pmatrix} \quad \text{and} \quad |2\rangle = \begin{pmatrix} -1 \\ 1 \\ 0 \\ 0 \end{pmatrix}. \tag{9}$$

Here, we represent the order parameter by a real-space state vector, where each row corresponds to the strength of the pairing potential in one of the distinct, symmetry related sites within the unit cell. We investigate the fate of this doubly degenerate instability by writing the order parameter as a linear combination $|\Delta\rangle = \eta_1|1\rangle + \eta_2|2\rangle$ in the doubly degenerate subspace and consider the GL free energy up to the quartic order. Here, η_1 and η_2 are complex coefficients. By minimizing the GL free energy, we find the three possible instabilities, corresponding to $(\eta_2, \eta_2) = (1, 0)$, $(1, 1)$ and $(1, i)$. The instability which breaks the TRS corresponds to $(\eta_2, \eta_2) = (1, i)$ and leads to the pairing potential

$$|\Delta\rangle = |1\rangle + i|2\rangle = \begin{pmatrix} -i \\ i \\ -1 \\ 1 \end{pmatrix}. \tag{10}$$

This ground state has finite Josephson currents within a unit cell of the system since the symmetry-related sites have nontrivial phase differences between them. Hence, the system spontaneously breaks TRS at the superconducting transition.

* Corresponding authors: tian.shang@psi.ch
† Corresponding authors: S.Ghosh@kent.ac.uk

[1] K. Cenzual and E. Parthié, "Zr_3Ir with tetragonal α-V_3S structure," Acta Cryst. C **41**, 820 (1985).

Table SIII. Normal- and superconducting state properties of Zr_3Ir, as determined from electrical resistivity, magnetic susceptibility, specific-heat, and μSR measurements, as well as band structure calculation. The London penetration depth λ_L, the effective mass $m^\star$, carrier density n_s, BCS coherence length ξ_0, electronic mean-free path l_e, Fermi velocity v_F, and effective Fermi temperature T_F were estimated following the Eqs. (40)–(50) in Ref. 19. The derived parameters are comparable to the previous results Ref. 12.

Property	Unit	Value
T_c [a]	K	2.2(1)
ρ_0	$\mu\Omega$cm	27.5(3)
$\mu_0 H_{c1}$	mT	12.7(2)
$\mu_0 {H_{c2}}^{\rho}$	T	1.08(1)
$\mu_0 {H_{c2}}^{C}$	T	0.62(1)
$\mu_0 H_p$	T	4.1(1)
$\xi(0)$	nm	23.0(2)
γ_n	mJ/mol-K^2	17.9(1)
Θ_D^C	K	220(5)
Θ_E^C	K	297(10)
λ_{ep}	—	0.57(10)
$N(\epsilon_F)$	states/eV-f.u.	3.80(1)
$N(\epsilon_F)^{DFT}$	states/eV-f.u.	2
E_{ASOC}	meV	100
${\Delta_0}^{\mu SR}$(clean)	meV	0.30(1)
${\Delta_0}^{\mu SR}$(dirty)	meV	0.23(1)
Δ_0^C	meV	0.32(1)
$\Delta C/\gamma_n T_c$	—	1.32(1)
$\lambda_0^{\mu SR}$	nm	294(2)
λ_{GL}	nm	182(2)
λ_L	nm	175(5)
κ	—	8.1(1)
$m^\star$	m_e	10.5(2)
n_s	10^{27} m^{-3}	9.6(5)
ξ_0	nm	50(4)
l_e	nm	28(1)
ξ_0/l_e	—	1.8(2)
v_F	10^4 ms^{-1}	7.2(3)
T_F	10^3 K	3.6(2)

[a] Similar values were determined via electrical resistivity, magnetic susceptibility, and heat-capacity measurements.

[2] C. Kittel, *Introduction to Solid State Physics*, 8th ed. (Wiley, New York, 2005).

[3] W. L. McMillan, "Transition temperature of strong-coupled superconductors," Phys. Rev. **167**, 331–344 (1968).

[4] R. Movshovich, M. Jaime, J. D. Thompson, C. Petrovic, Z. Fisk, P. G. Pagliuso, and J. L. Sarrao, "Unconventional superconductivity in $CeIrIn_5$ and $CeCoIn_5$: Specific heat and thermal conductivity studies," Phys. Rev. Lett. **86**, 5152–5155 (2001).

[5] M. Tinkham, *Introduction to superconductivity*, 2nd ed. (Dover, New York, 1996).

[6] N. R. Werthamer, E. Helfand, and P. C. Hohenberg, "Temperature and purity dependence of the superconducting critical field, H_{c2}. III. Electron spin and spin-orbit effects," Phys. Rev. **147**, 295–302 (1966).

[7] F. Kneidinger, H. Michor, A. Sidorenko, E. Bauer, I. Zeiringer, P. Rogl, C. Blaas-Schenner, D. Reith, and R. Podloucky, "Synthesis, characterization, electronic structure, and phonon properties of the noncentrosymmetric superconductor LaPtSi," Phys. Rev. B **88**, 104508 (2013).

[8] D. C. Peets, A. Maldonado, M. Enayat, Z. Sun, P. Wahl, and A. P. Schnyder, "Upper critical field of the noncentrosymmetric superconductor BiPd," Phys. Rev. B **93**, 174504 (2016).

[9] N. Kimura, N. Kabeya, K. Saitoh, K. Satoh, H. Ogi, K. Ohsaki, and H. Aoki, "Type II/1 superconductivity with extremely high H_{c3} in noncentrosymmetric $LaRhSi_3$," J. Phys. Soc. Jpn. **85**, 024715 (2016).

[10] V. K. Anand, D. Britz, A. Bhattacharyya, D. T. Adroja, A. D. Hillier, A. M. Strydom, W. Kockelmann, B. D. Rainford, and K. A. McEwen, "Physical properties of noncentrosymmetric superconductor $LaIrSi_3$: A μSR study," Phys. Rev. B **90**, 014513 (2014).

[11] M. Smidman, A. D. Hillier, D. T. Adroja, M. R. Lees, V. K. Anand, R. P. Singh, R. I. Smith, D. M. Paul, and G. Balakrishnan, "Investigations of the superconducting states of noncentrosymmetric $LaPdSi_3$ and $LaPtSi_3$," Phys. Rev. B **89**, 094509 (2014).

[12] Sajilesh K. P., D. Singh, P. K. Biswas, Gavin B. G. Stenning, A. D. Hillier, and R. P. Singh, "Investigations of the superconducting ground state of Zr_3Ir: Introducing a new noncentrosymmetric superconductor," Phys. Rev. Materials **3**, 104802 (2019).

[13] J. P. Perdew, K. Burke, and M. Ernzerhof, "Generalized gradient approximation made simple," Phys. Rev. Lett. **77**, 3865 (1996).

[14] G. Kresse and J. Furthmüller, "Efficient iterative schemes for ab initio total-energy calculations using a plane-wave basis set," Phys. Rev. B **54**, 11169 (1996).

[15] G. Kresse and J. Furthmüller, "Efficiency of ab-initio total energy calculations for metals and semiconductors using a plane-wave basis set," Comput. Mater. Sci. **6**, 15 (1996).

[16] G. Kresse and D. Joubert, "From ultrasoft pseudopotentials to the projector augmented-wave method," Phys. Rev. B **59**, 1758 (1999).

[17] P. E. Blöchl, "Projector augmented-wave method," Phys. Rev. B **50**, 17953 (1994).

[18] S. Ghosh, J. F. Annett, and J. Quintanilla, "Time-reversal symmetry breaking in superconductors through loop josephson-current order," arXiv preprint arXiv:1803.02618 (2018).

[19] J. A. T. Barker, B. D. Breen, R. Hanson, A. D. Hillier, M. R. Lees, G. Balakrishnan, D. McK. Paul, and R. P. Singh, "Superconducting and normal-state properties of the noncentrosymmetric superconductor Re_3Ta," Phys. Rev. B **98**, 104506 (2018), and references therein.